Northumbria Research Link

Northumbria
University
NEWCASTLE

University Library

PAPER

P-type conductivity in Sn-doped Sb$_2$Se$_3$

Theodore D C Hobson[1,8,*] ⓘ, Huw Shiel[1,2,8], Christopher N Savory[3], Jack E N Swallow[1,4], Leanne A H Jones[1,4], Thomas J Featherstone[1], Matthew J Smiles[1] ⓘ, Pardeep K Thakur[5], Tien-Lin Lee[5], Bhaskar Das[6], Chris Leighton[6], Guillaume Zoppi[7] ⓘ, Vin R Dhanak[1], David O Scanlon[3], Tim D Veal[1] ⓘ, Ken Durose[1] ⓘ and Jonathan D Major[1]

1   Stephenson Institute for Renewable Energy and Department of Physics, University of Liverpool, L69 7ZF Liverpool, United Kingdom
2   Department of Materials, Imperial College London, SW7 2BP London, United Kingdom
3   Department of Chemistry, University College London, 20 Gordon Street, WC1H 0AJ London, United Kingdom
4   Department of Materials, University of Oxford, Parks Road, OX1 3PH Oxford, United Kingdom
5   Diamond Light Source, Harwell Science & Innovation Campus, OX11 0DE Didcot, United Kingdom
6   Department of Chemical Engineering & Materials Science, University of Minnesota, Minneapolis, MN, United States of America
7   Department of Mathematics, Physics & Electrical Engineering, Northumbria University, Newcastle upon Tyne, United Kingdom
8   These authors contributed equally to this work.
*   Author to whom any correspondence should be addressed.

E-mail: thobson@liverpool.ac.uk

Abstract

Antimony selenide (Sb$_2$Se$_3$) is a promising absorber material for thin-film photovoltaics. However, certain areas of fundamental understanding of this material remain incomplete and this presents a barrier to further efficiency gains. In particular, recent studies have highlighted the role of majority carrier type and extrinsic doping in drastically changing the performance of high efficiency devices (Hobson *et al* 2020 *Chem. Mater.* **32** 2621–30). Herein, Sn-doped Sb$_2$Se$_3$ bulk crystals are shown to exhibit p-type conductivity using Hall effect and hot-probe measurements. The measured conductivities are higher than those achieved through native defects alone, but with a carrier density (up to 7.4×10^{14} cm^{-3}) several orders of magnitude smaller than the quantity of Sn included in the source material. Additionally, a combination of ultraviolet, x-ray and hard x-ray photoemission spectroscopies are employed to obtain a non-destructive depth profile of the valence band maximum, confirming p-type conductivity and indicating a majority carrier type inversion layer at the surface. Finally, these results are supported by density functional theory calculations of the defect formation energies in Sn-doped Sb$_2$Se$_3$, showing a possible limit on the carrier concentration achievable with Sn as a dopant. This study sheds light on the effectiveness of Sn as a p-type dopant in Sb$_2$Se$_3$ and highlights avenues for further optimisation of doped Sb$_2$Se$_3$ for solar energy devices.

1. Introduction

The emergence of Sb$_2$Se$_3$ as a thin film solar absorber has caused great excitement in the field of next-generation photovoltaics (PV) due to its low-cost earth-abundant constituent elements and its excellent opto-electronic properties [1]. However, there is still some uncertainty over several fundamental properties of this material that must be solved before Sb$_2$Se$_3$ can be taken from promising to a potentially market-competitive material [2]. Some of the most significant questions involve the defect properties of the material [3, 4] and how they affect the native majority carrier type and the potential for doping it either n- or p-type for forming the most efficient device structures. Sb$_2$Se$_3$ is generally considered to be a p-type semiconductor and previous studies have evidenced this [5]. However, some studies suggest that without extrinsic dopants, Sb$_2$Se$_3$ is difficult to dope strongly n- or p-type [6]. It has previously been shown that the presence of unintended Cl contamination in purchased source material caused strong n-type conductivity and the formation of an isotype n-n$^+$ junction between Sb$_2$Se$_3$ and a TiO$_2$ window layer [7]. These isotype

devices performed comparably to the more widely reported nominal p–n junctions [8], suggesting that performance gains could be attainable through careful control of majority carrier type. P-type Sb_2Se_3 should provide improved open circuit voltages, while good control of the doping is crucial for effective device optimisation and reproducibility. This study aims to investigate the potential for doping Sb_2Se_3 with Sn, another cheap and earth-abundant metal. To do this, we utilised bulk crystal samples grown from high-purity starting materials, either undoped, or intentionally doped with a known quantity of Sn. This allowed us to limit the impact of unintentional impurities and grain boundaries, which may affect the observed doping behaviours in thin films.

Tin doping has clear appeal as a route to achieve p-type conductivity in Sb_2Se_3. Sn has a similar atomic radius to Sb, while, being a group-IV element to Sb's group-V and having a similar tendency to exhibit lone pair behaviour (see section 3.3 below), one may expect it to act as an acceptor if it were to occupy a Sb site within Sb_2Se_3. Previous experimental work with bulk crystals of Sb_2Se_3 has suggested that Sn does, indeed, induce p-type conductivity [9], while theoretical modelling has suggested that Sn_{Sb} impurities ought to act as shallow acceptors [10]. Recently, Sn doping was utilised to form the p-type layer in a Sb_2Se_3 homojunction device, with p-type conductivity in the Sn-doped layer confirmed by Hall effect measurements [11].

A notable property of Sb_2Se_3 is its unusual one-dimensional nanoribbon structure. Covalently-bonded chains extend in the [001]-direction (using the *Pbnm* space group setting [12]), with van der Waals interactions holding the nanoribbons together in the other two directions. In previous studies it has been shown that large bulk crystals of Sb_2Se_3 can be fabricated using the Bridgman melt-growth method and that these crystals cleave easily in the (010) plane [7, 13]. This allowed for *in situ* cleaving or exfoliating under ultra-high vacuum, providing a pristine, uncontaminated surface for photoemission measurements [13]. In this study, different types of photoemission measurements with different levels of surface sensitivity are employed to acquire a depth profile of the valence band maximum (VBM) to Fermi level (E_F) separation and find a solution to Poisson's equation for surface space charge layers.

2. Methods

2.1. Crystal growth
The Sb_2Se_3 bulk crystals utilised in this work were prepared via the Bridgman melt-growth technique, using a single-zone vertical furnace. Pure undoped Sb_2Se_3 source material was first prepared separately from Sb (99.9999%, Alfa Aesar) and Se (99.999%, Alfa Aesar) shot, with a small excess (0.01 mol%) of Sb or Se included, with the former denoted 'Se-poor' and the latter 'Se-rich'. In addition to crystals prepared from Sb_2Se_3 source material synthesised on site, crystals were also grown from 'as-purchased' Sb_2Se_3 granulate, synthesised by the manufacturer (99.999%, Alfa Aesar). In previous reports, source material as-purchased from this supplier was shown to contain Cl impurities that induced n-type conductivity in crystals that were not intentionally doped [7]. Sb_2Se_3 source material (whether prepared on-site or as-purchased) was ground using a pestle and mortar with 0.1 mol% of Sn powder included for doped samples and placed in a quartz tube. Assuming all the Sn was incorporated substitutionally, this would produce a density of Sn atoms of 7×10^{18} cm^{-3}, but this could not be directly measured. The tubes were flushed three times with Ar gas then evacuated to $\sim 10^{-5}$ mbar to evaporate residual volatile compounds. The tubes were filled with Ar at a pressure of 100 mbar immediately before sealing, intended to suppress the sublimation of Sb_2Se_3 that occurs at low pressure due to the high vapour pressure of Sb_2Se_3 [14]. This was necessary to avoid the formation of large gas bubbles in the crystal boules and also to prevent unwanted vapour transport of material away from the melt-grown crystals. The sealed ampoules were placed with the bottom tip in line with the peak of the temperature profile in the furnace and heated to 620 °C (the melting point of Sb_2Se_3 is 611 °C). They were then held for around 6 h to allow full melting and homogenisation of the powder. The ampoules were then lowered through the natural temperature gradient of the furnace, at 0.6 °C mm^{-1} in the working range, towards the lower, open end of the furnace (at room temperature), at a rate of 1.15 mm h^{-1} for seven days. The ampoules were rotated at around 0.2 Hz throughout to ensure homogeneous heating.

2.2. Crystal characterisation
Sections of Sb_2Se_3 bulk crystal were manually cleaved to produce a flat, clean surface for characterisation. Previous studies have identified this as the (010) crystal plane [15] (*Pbnm* setting). Powder x-ray diffraction (XRD) was carried out in θ–2θ step-scan mode with a Rigaku Smartlab Diffractometer using the monochromated Cu K-α_1 line (1.5406 Å) with a resolution of 0.01°. Qualitative secondary ion mass spectroscopy (SIMS) measurements were carried out on the (010) surface using a Hiden Analytical gas ion gun and quadrupole detector. O$^-$ ions were used at 5 keV beam energy and 300 nA current, with a scan area of approximately 0.5×0.5 mm^2. A data gating area of 10% was used to remove side-wall effects.

For hot-probe measurements, two lateral 100 nm thick Au contacts were deposited via thermal evaporation onto the (010) plane with areas varying from 0.03 to 0.1 cm^2 depending on the size and shape of the crystals. The ionisation potential of Sb_2Se_3 has been estimated at 5.26 eV [7], which suggests the work function for p-Sb_2Se_3 is smaller than the work function of Au (5.31–5.47 eV) [16], meaning that Au ought to produce Ohmic contacts in this case, assuming the crystals were p-type. Hot-probe measurements were carried out using a Keithley 2400 source meter with Au wire probes. A heat source was applied to one probe during measurement, with its temperature monitored by a K-type thermocouple. After the principal measurement, the sample was allowed to cool and the heat source was applied to the opposite probe (without temperature monitoring) to confirm that an opposite current flowed and that currents were thermally-induced. Immediately prior to measurement of Sb_2Se_3, n-InSb and p-CdTe reference samples were measured with the hot-probe, in order to assign a current polarity for each conductivity type given the probe setup. The same probe configuration was then used for the Sb_2Se_3 crystals.

For capacitance–voltage (*C*–*V*) measurements, one In and one Au contact, both thermally evaporated at a thickness of 100 nm, were used, with the In contact intended to act as Schottky barrier and the Au as an Ohmic contact (assuming p-type crystals). *C*–*V* measurements were carried out with a Solartron 1260 Frequency Response Analyser and 1296 Dielectric Interface at a range of AC frequencies from 7.1 kHz to 12.6 kHz, with DC bias from −1 to +1 V at room temperature in the dark.

Hall effect measurements were carried out in the van der Pauw geometry using sputtered 100 nm thick Au contacts. Measurements were made using a Keithley 2400 source meter and a Quantum Design Physical Property Measurement System. Applied magnetic field strengths of up to 90 kOe (equivalent to 9 T) were used and all measurements were taken at 300 K. All the typical inversions of excitation current and magnetic field were employed, and a zero-field background was subtracted

2.3. Photoemission

Hard x-ray photoemission spectroscopy (HAXPES) data were acquired at the Diamond Light Source facility using the I09 beamline. Hard x-rays with an energy of 5921 eV were monochromated using a Si(111) double-crystal followed by a Si(004) channel-cut crystal. Measurements were carried out on bulk Sn-doped Sb_2Se_3 crystals with Se-rich stoichiometry, cleaved *in situ* by knocking a peg attached to the crystal with epoxy with a wobble stick to expose a pristine surface. The base pressure of the measurement chamber was $\sim 10^{-10}$ mbar. Photoelectrons were collected by a Scienta Omicron EW4000 high-energy analyser with an acceptance angle of $\pm 28°$. The energy resolution was determined to be 0.25 eV by fitting a Gaussian-broadened Fermi–Dirac distribution to the Fermi edge of a Au reference sample. Lab-based x-ray photoemission spectroscopy (XPS) was performed using a SPECS monochromatic Al K-α source ($h\nu =$ 1486.6 eV) and data were collected with a PSP Vacuum Technologies hemispherical electron-energy analyser with an acceptance angle of $\pm 3°$. The base pressure of the measurement chamber was $\sim 10^{-10}$ mbar. The energy resolution was 0.45 eV, determined from the Fermi edge of a Ag reference sample. Ultraviolet photoemission spectroscopy (UPS) was performed using the same analyser setup as for XPS and a He(I) ultraviolet lamp. Energy resolution was determined to be 0.12 eV by fitting a Gaussian-broadened Fermi–Dirac distribution to the Fermi edge of a Ag reference sample. Photoemission spectra were curve fitted using CASAXPS software with Voigt lineshapes after subtracting a Shirley background [17]. The HAXPES and lab-based photoemission techniques were carried out on pieces of crystal from the same sample, and the UPS and XPS were performed on the same sample, without breaking vacuum in between the two measurements.

2.4. Computational details

All density functional theory (DFT) calculations were performed within periodic boundary conditions using the Vienna *Ab initio* Simulation Package, [18–21] in which the interaction between valence and core (Sb: [Kr] $4d^{10}$, Se: [Ar] $3d^{10}$ and Sn: [Kr]) electrons was described by the projector augmented wave method [22], with scalar-relativistic pseudopotentials. The calculations in this work utilised the same method that has been used in previous studies on the defects of Sb_2Se_3 to provide parity with the results from those studies: [6, 7] the Heyd, Scuseria and Ernzerhof (HSE06) [23, 24] was used as exchange correlation functional with the inclusion of the D3 dispersion correction of Grimme [25] was used for all calculations, which has been demonstrated to simulate the structural and electronic properties of the compound—the density of state (DOS) calculations are described in that work [26]. Defect calculations were performed on a $1 \times 3 \times 1$ supercell (60 atoms) with a plane-wave energy cutoff of 350 eV and a Γ centred $2 \times 2 \times 2$ k-point mesh. Calculations of Sn metal and all competing Sn–Sb and Sn–Cl phases to predict the chemical potential limits of extrinsic Sn-doping were performed using the same cutoff energy and a k-point mesh converged for each material such that the predicted total energy changed by no more than 1 meV per atom. Defect and geometry optimisations of competing phases used convergence criterions of 1×10^{-5} eV on the total energy and

$0.01\,\text{eV}\,\text{Å}^{-1}$ on the forces per atom. Consistent with the approach taken in previous studies, three finite size corrections were included to restore the dilute defect model and correct the defect formation energies: an alignment of the electrostatic potential of host and defect supercells [27], a 'band-filling' correction for shallow states [28] and the Murphy and Hine implementation of the Lany–Zunger 'image charge' correction, accounting for the highly anisotropic dielectric constant of Sb_2Se_3 [29].

2.5. Methodology for solving the Poisson equation

A python script was used to model the surface space charge profile of Sb_2Se_3 using the modified Thomas–Fermi approximation [30]. Specific conditions for the bulk Fermi level position and the amount of band bending were informed by the photoemission data and a solution to Poisson's equation was found using an iterative interval bisection method. Full details are provided elsewhere [31].

3. Results

3.1. Crystal doping

Upon removal from the growth tubes, the mechanical properties of the Sb_2Se_3 crystals were consistent with those that have been reported in previous work where this growth method was used, i.e. crystals were found to cleave easily along a single plane to produce large, reflective facets [7, 13, 15, 32]. The crystallographic properties of Sb_2Se_3 bulk crystals grown by this technique have been documented in other studies via XRD [12, 15], and it was considered reasonable to assume that the crystals reported in this study shared these properties. No visual differences were observed between the crystals grown from Se-poor, Se-rich or as-purchased Sb_2Se_3, as can be seen from figure S1 in the supporting information. Additionally, figures S2(a) and(b) show that the XRD patterns from powdered sections of a Sn-doped Se-rich crystal and a crystal grown from as-purchased Sb_2Se_3 were essentially identical to the pattern for an undoped stoichiometric crystal (this last sample was not analysed further in this work). Not every sample in this work was analysed via powder XRD, but these results suggest that the small differences in the stoichiometry and impurity content of these crystals did not introduce any significant structural changes. Qualitative SIMS measurements were carried out to determine if Sn had incorporated into the bulk crystal, with results shown in figure 1 for a Sn-doped crystal, compared to an undoped crystal, (i.e. grown under the same conditions but without Sn added to the growth tube). Although the results could not be quantified without implanted standards, the sputter time is likely to represent a depth of several 10 s of μm, and the significantly higher count rate for Sn in the doped crystal suggests effective incorporation of Sn into the crystal, rather than segregation (the spike near 0 s is due to the SIMS surface transient effect and is not representative of surface composition). Additionally, given that the SIMS was uncalibrated, the slight downward slope of the profile towards greater depth in the Sn-doped sample is not necessarily indicative of any real change in concentration with depth. The implication of a concentration gradient for Hall effect and *C*–*V* measurements would mean that the measured carrier densities would represent an average over a given depth, while for photoemission measurements the surface sensitivity is far removed from the length scales probed by SIMS. However, for the purposes of this work, the SIMS is treated solely as qualitative evidence of Sn doping.

3.1.1. Hot-probe measurements

Hot-probe measurements were carried out on both Sn-doped and undoped Sb_2Se_3 crystals that were grown from as-purchased, Se-poor and Se-rich source materials. A summary of the results is shown in in table 1 while the raw hot-probe data are shown in figure 2. The table also shows estimates of the resistivities of the samples obtained from two-terminal source-meter measurements. First, the undoped samples: previous studies have reported n-type conductivity in crystals grown from the as-purchased Sb_2Se_3 due to unintentional Cl [7], presumably present as Cl_{Se}, and this is included in table 1 for reference. In contrast, the Se-rich material grown from ultra-pure elements in this study showed p-type conductivity, as would be expected from the intrinsic acceptor V_{Sb}. However, no meaningful thermo-current could be obtained from the Se-poor sample (figure 2) and since it was also highly resistive, we could not determine the majority carrier type (this was despite the fact that a sample of this type may naively be expected to be measurably n-type due to V_{Se}). Second, the doped samples: all showed p-type behaviour regardless of the origin of the material and its stoichiometry. The as-purchased material had thus been converted from its original n- to p-type conductivity by the Sn-doping. The Se-rich material retained its p-type character but became more conductive, while the Se-poor material transitioned from unmeasurable to being measurably p-type and became more conductive. Overall, the resistivities of the samples followed the trends of the magnitudes of the thermo-currents, giving some confidence that the observed effects were indeed caused by the intentional changes made to doping and stoichiometry.
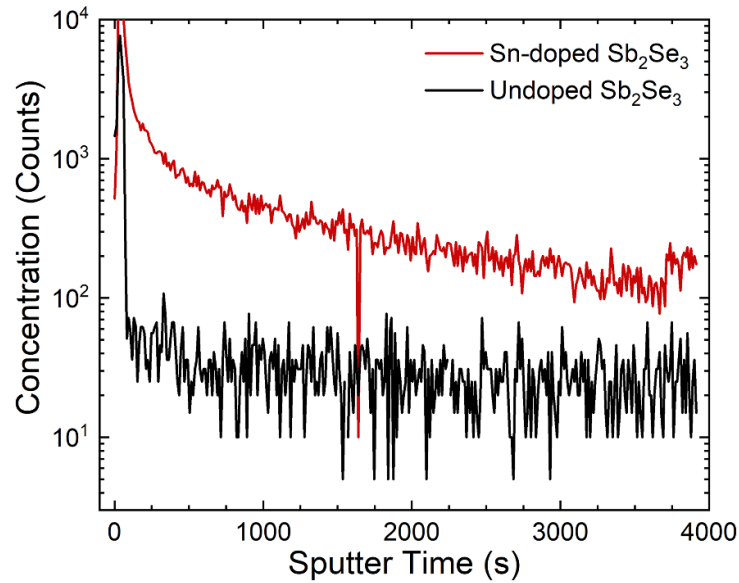
Figure 1. SIMS measurements (uncalibrated) of Sn-doped and undoped Sb_2Se_3 crystals for Sn-120. Depths probed are expected to be on the order of 10 s of μm. Tabulated data available at [33].

Table 1. Majority carrier type (from hot-probe) and resistivities (two-terminal measurement) of Sb_2Se_3 bulk crystals.

Sb_2Se_3 source material	Dopant	Conductivity type	Resistivity (kΩ cm)
Se-poor from elements	Undoped	Unmeasurable	1.3×10^5
Se-rich from elements	Undoped	p-type	2.5×10^2
As-purchased[a]	Undoped	n-type	4.9
Se-poor from elements	Sn	p-type	4.4×10^3
Se-rich from elements	Sn	p-type	6.9
As-purchased	Sn	p-type	10

[a] The data for the undoped sample grown from 'as-purchased' Sb_2Se_3 are taken from [7] and are included here for comparison, while the others are original to this work.

3.1.2. Capacitance–voltage measurements

Capacitance–voltage measurements allow the net density of ionised donors and acceptors in a sample to be estimated. If an appropriate AC frequency range is selected where capacitance is constant with frequency, bound charges can be excluded, allowing a measurement of carrier density [34]. First principles calculations of the effective DOS in the conduction and valence bands of Sb_2Se_3 [35] suggest that at 300 K, an intrinsic carrier density of the order 10^8 would be expected (assuming a bandgap of 1.2 eV), so any values higher than this would result from either native defects or extrinsic dopants. Despite largely being measurable via hot-probe, for all samples besides the Sn-doped Se-rich, the resistivity was too high for meaningful *C–V* measurements (see figure S3 for more details). Figure S3(a) shows *C–f* measurements taken for the Sn-doped Se-rich sample to establish a suitable frequency range at which Mott–Schottky plots could be taken. Based on this, *C–V* measurements were carried out at a range of frequencies in the vicinity of 100 kHz. This range was selected because for frequencies higher than these, the capacitance signal was very low, approaching the detection limit for the equipment (1 pF) and producing high noise levels. At frequencies below this range, it was expected that bound charges from carrier traps would contribute to the carrier density estimate, reducing its accuracy [34]. A representative Mott–Schottky plot derived from the *C–V* scan taken at 100 kHz is shown in figure 3(a) which exhibits behaviour expected for a Schottky junction in series with an Ohmic contact. From Mott–Schottky plots such as this, carrier density values were derived from the gradient at reverse bias. These results can be seen in figure 3(b), where the measured carrier density did not vary significantly with measurement frequency in the range 100–130 kHz. Given this, a carrier density value of 2×10^{14} cm^{-3} is estimated from the *C–V* measurements.

3.1.3. 300 K Hall effect measurements

Hall effect measurements were successfully carried out on Sn-doped crystal samples, despite the high resistivities estimated from the two-terminal source meter measurements during the hot-probe measurements (see table 1). The results for the Se-poor Sn-doped crystal are shown in figure 4(a), where a
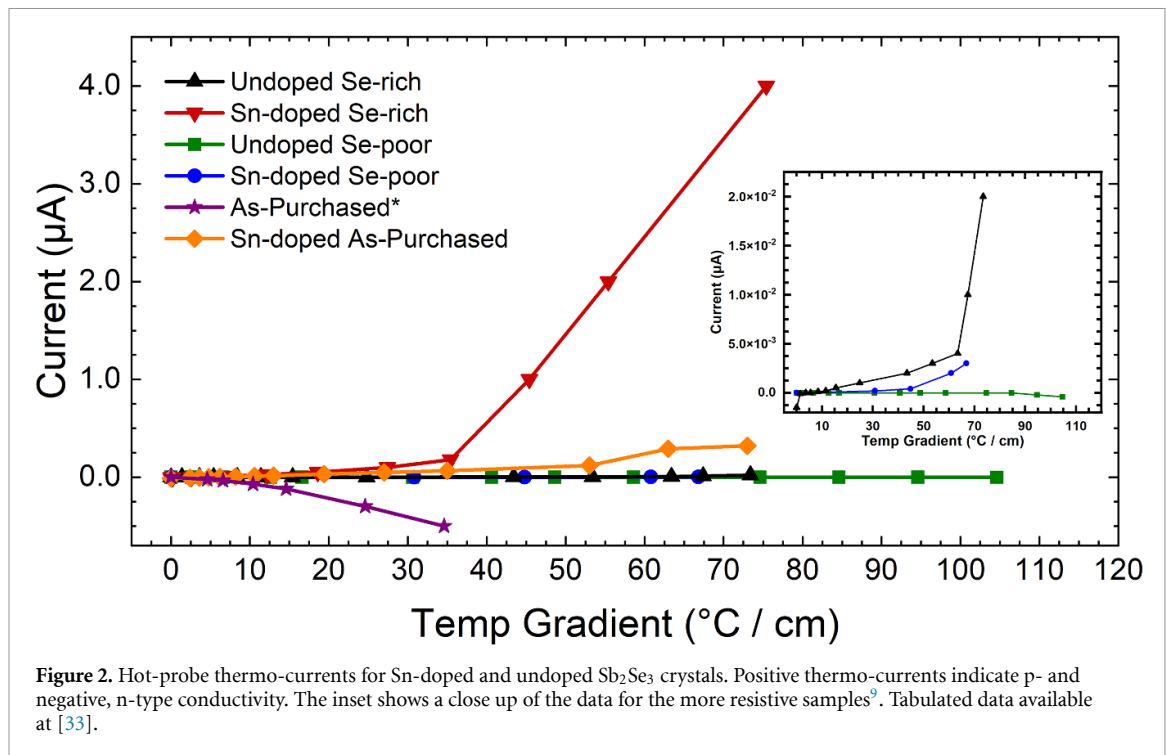
Figure 2. Hot-probe thermo-currents for Sn-doped and undoped Sb_2Se_3 crystals. Positive thermo-currents indicate p- and negative, n-type conductivity. The inset shows a close up of the data for the more resistive samples[9]. Tabulated data available at [33].
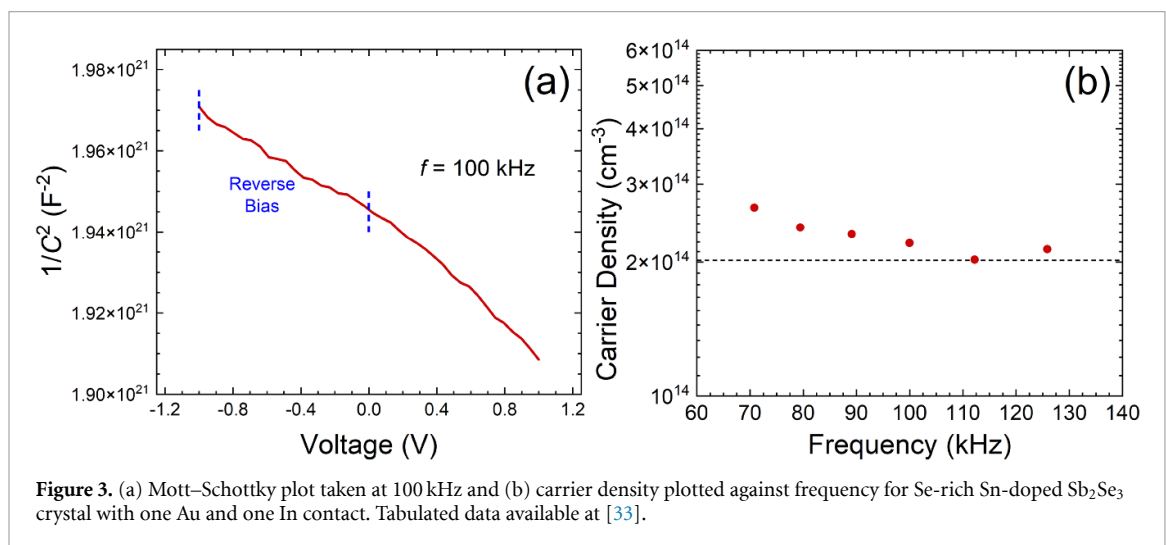

Figure 3. (a) Mott–Schottky plot taken at 100 kHz and (b) carrier density plotted against frequency for Se-rich Sn-doped Sb_2Se_3 crystal with one Au and one In contact. Tabulated data available at [33].

positive gradient (and so a positive Hall coefficient) indicates p-type conductivity, in agreement with the hot-probe results and theory (see section 3.3). The extracted hole density (see table 2) was low, at 7.5×10^{11} cm^{-3}, leading to a high resistivity, matching the resistivity order of magnitude estimated from the two-terminal source meter measurement (see table 1). These results suggest a low Sn-dopant activation ratio for Se-poor conditions. For the Se-rich sample (figure 4(b)), p-type majority carriers were also confirmed, while a larger hole density of 7.4×10^{14} cm^{-3} was observed, consistent with the lower resistivity (1.3 kΩ cm) of this sample. This result is broadly consistent with the results from *C–V*, lending confidence to the estimates from both measurements.

Finally, the Hall data for the Sn-doped crystal grown from as-purchased Sb_2Se_3 (figure 4(c)) showed p-type behaviour and a hole density of 3.0×10^{13} cm^{-3}. Once again, this is consistent with the hot-probe results, suggesting that despite the Cl impurities present in the sample, the larger quantity of Sn compensated these donors and inverted the majority carrier type. The residual donors from Cl contamination may explain the hole density being lower than the Se-rich crystal (which did not have significant Cl contamination), but since the stoichiometry of the as-purchased Sb_2Se_3 was not known, the influence of native defects cannot be

---

[9] As-purchased data was taken from [7] and is included here for reference.
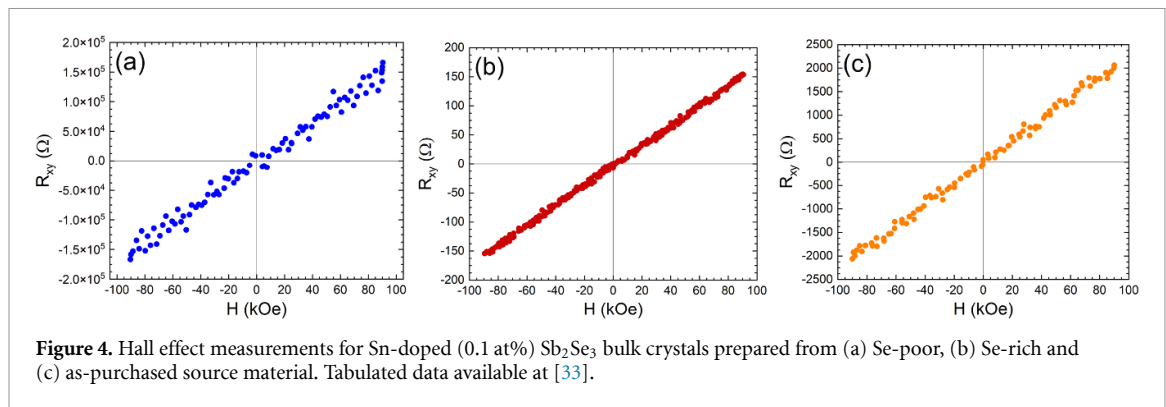
Figure 4. Hall effect measurements for Sn-doped (0.1 at%) Sb_2Se_3 bulk crystals prepared from (a) Se-poor, (b) Se-rich and (c) as-purchased source material. Tabulated data available at [33].

Table 2. 300 K Hall effect results for 0.1 at% Sn-doped Sb_2Se_3 bulk crystals. Cl contamination was present in 'as-purchased' material.

Sb_2Se_3 source material	ρ (kΩ cm)	p (cm^{-3})	μ (cm^2 V^{-1} s^{-1})
Se-poor from elements	1.7×10^3	7.5×10^{11}	4.9
Se-rich from elements	1.3	7.4×10^{14}	6.4
As-purchased	33	3.0×10^{13}	8.1

ruled out either. Regardless, the Hall results indicate that the main reason for the different conductivities of these samples are the different carrier densities, demonstrating the effectiveness of Sn-doping. However, the highest carrier density observed, at 7.4×10^{14} cm^{-3}, represents a low activation ratio, given that approximately 7×10^{18} cm^{-3} Sn atoms were expected in this sample.

Also important to note is that the extracted hole mobilities in table 2 are 4.9, 6.4, and 8.1 cm^2 V^{-1} s^{-1} for the three samples studied. This is significantly above the approximate mobility range (0.1–1 cm^2 V^{-1} s^{-1}) where the onset of hopping (rather than diffusive) transport is known to be capable of artificially inverting both Hall effect and thermopower signals [36]. This provides strong evidence that the p-type signals seen here in hot-probe and Hall measurement should be taken at face value. The extracted hole mobilities can also be compared to literature on Sb_2Se_3, where values as high as 20–40 cm^2 V^{-1} s^{-1} have been reported [1], though not for samples that were highly doped. The lower carrier mobilities observed in this work may be down to the high density of native defects and/or impurities expected in these samples, which may act as carrier traps and reduce the mobility.

3.2. Photoemission

Photoemission measurements were carried out with three techniques of different surface sensitivity on Sn-doped Sb_2Se_3 crystals with Se-rich stoichiometry. The inelastic mean free path (IMFP) of electrons through a given material is dependent on their kinetic energy and this can be calculated using the so-called TPP-2M equation [37]. The IMFP vs energy relationship for Sb_2Se_3 is shown in figure S4 in the supporting information.

The core levels of Sn were not observed in XPS scans covering the relevant energy range (not shown), but this is not surprising, since the concentration of 0.1 at% is expected to lie below the detection limit for core levels. The valence band spectra of the doped crystal as measured by UPS, XPS and HAXPES are shown in figure 5. The VBM values determined from these spectra were used to find a solution to Poisson's equation that fits the photoemission data, shown in figure 6(a). Initially, the VBM-E_F separations for the valence bands in figure 5 were determined by finding the intercept of straight lines fitted to the steepest part of the valence band edge and the flattest part of the background (figure S5). However, the difference in the instrumental resolution between the three photoemission techniques means that this linear fit approximation of the band edge is not consistent, and this was observed in the difficulty to achieve a solution to Poisson's equation that fits all three data points (see figure S6). Therefore, while the linear extrapolation method is commonplace in VBM estimation, in instances such as this, where different instruments and radiation sources have been used, a more thorough approach is required to determine the valence band edge maximum.

DFT-calculated DOS can be aligned to the valence band data acquired from photoemission measurements to achieve a good fit. This data is broadened using the known Gaussian instrumental broadening of the technique used (as well as the Lorentzian lifetime broadening). The DOS is calculated by DFT with the VBM at 0 eV, meaning that whatever shift is necessary to fit the DOS to the data is a good measurement of the true VBM-E_F separation. The total shift required to fit the DOS to the data is included alongside a straight line in figures 5(a)–(c) to show this point on the *x*-axis.
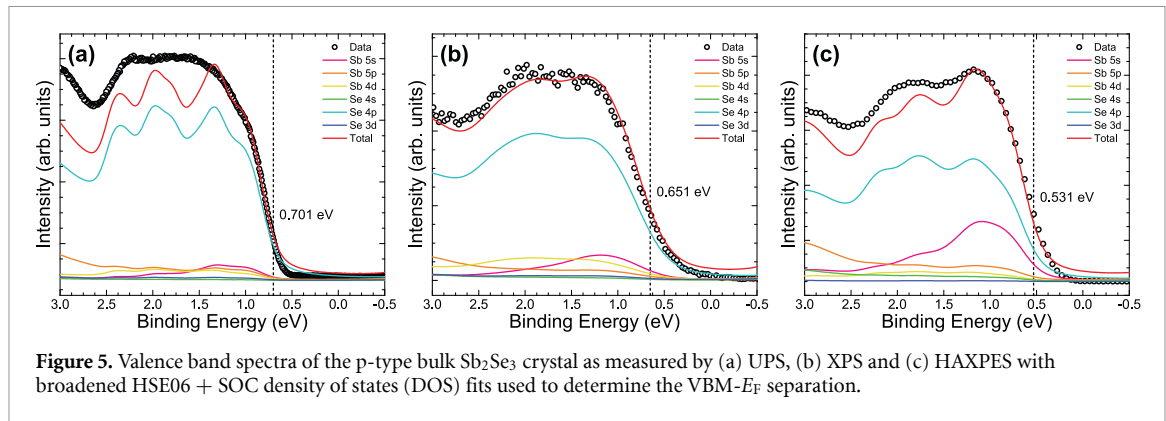
Figure 5. Valence band spectra of the p-type bulk Sb_2Se_3 crystal as measured by (a) UPS, (b) XPS and (c) HAXPES with broadened HSE06 + SOC density of states (DOS) fits used to determine the VBM-E_F separation.
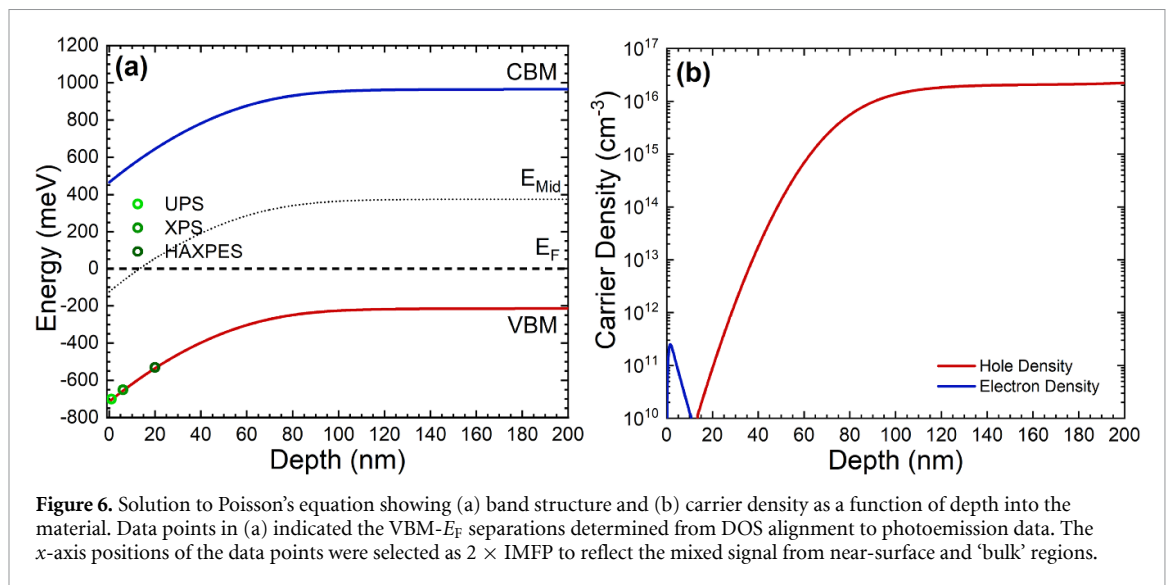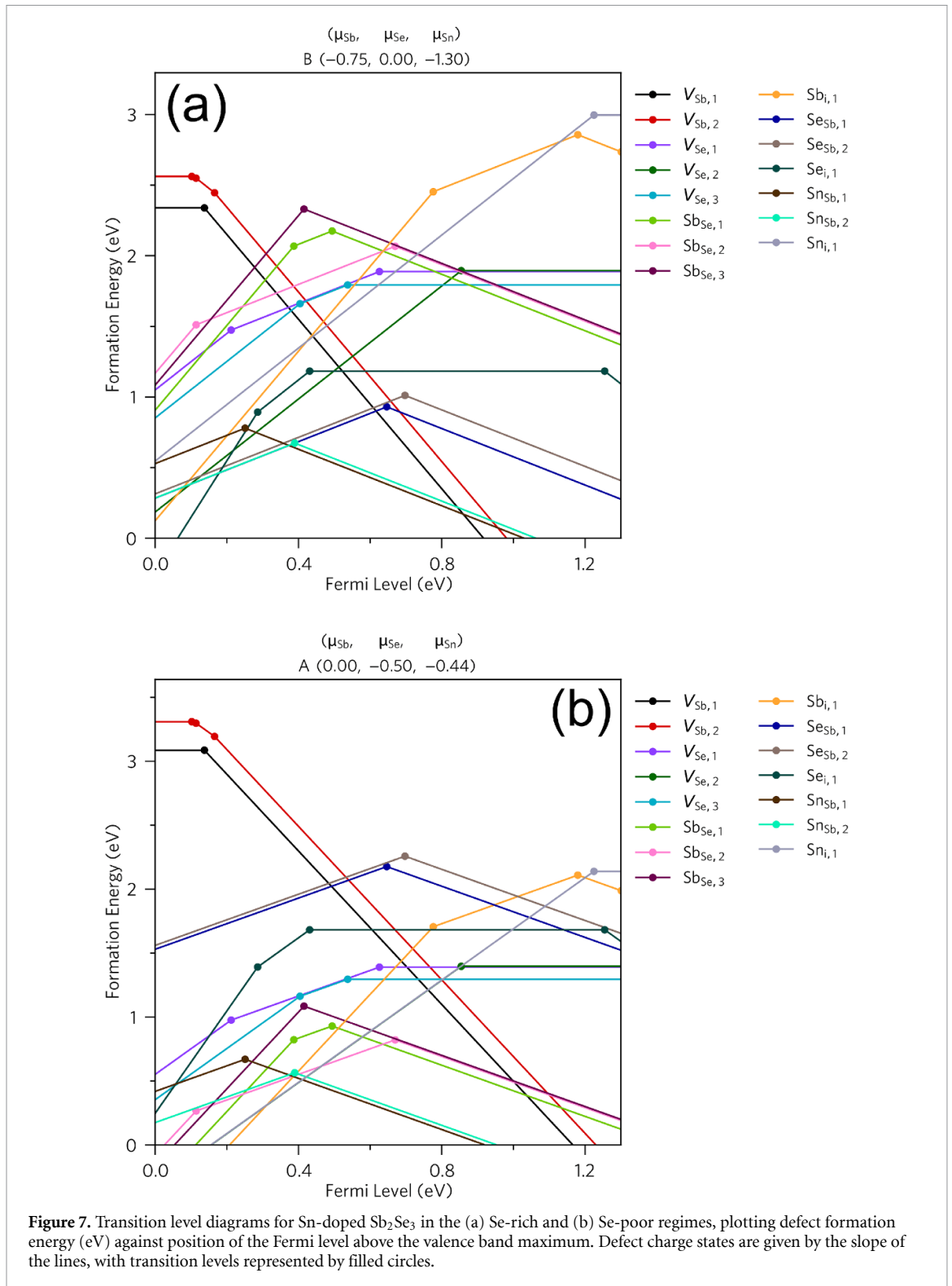

Figure 6. Solution to Poisson's equation showing (a) band structure and (b) carrier density as a function of depth into the material. Data points in (a) indicated the VBM-E_F separations determined from DOS alignment to photoemission data. The *x*-axis positions of the data points were selected as 2 × IMFP to reflect the mixed signal from near-surface and 'bulk' regions.

It is clear from examining figure 5 that the difference between the 'foot' of the valence band and the true position of the VBM is particularly pronounced for the XPS data, whereas it is reasonably similar for UPS and HAXPES. This supports the theory that the fit in figure S5 is poor due to the lower resolution of lab-based XPS. The measured binding energies of 0.701 eV, 0.651 eV and 0.531 eV for UPS, XPS and HAXPES respectively present some interesting results. While the HAXPES result of 0.531 eV indicated p-type conductivity (lying below the mid-gap energy), the UPS and XPS results evidence weakly n-type conductivity or insulating behaviour in the near surface region. This indicates a majority carrier type inversion layer with the transition from p-type to n-type conductivity taking place ∼13 nm deep in the material, as indicated in figure 6(b). This may have implications for the interpretation of the electrical measurements (see section 4). The Poisson equation was solved to fit these new VBM energies, as shown in figure 6(a), achieving a good fit to the three data points. The bulk Fermi level position required for this fit was 0.215 eV above the VBM, corresponding to a bulk hole density of 2.06×10^{16} cm^{-3}. The total amount of band bending was 500 meV. It should be noted that this band-bending is not related to the spike and slope observed in the Sn concentration in SIMS, which covers a ∼10 μm depth scale, in contrast to the 10 s of nm scale of the photoemission measurements.

3.3. DFT
All measurements, to differing degrees, show a lower carrier concentration than would naively be expected from the quantity of Sn incorporated into the crystal. About 0.1 at% of Sn with 100% activation would lead to carrier densities in the region of 7×10^{18} cm^{-3}, far higher than the 10^{13}–10^{16} cm^{-3} estimated in this work. To better understand this, DFT was used to calculate the formation energies of different defect states in Sn-doped Sb_2Se_3. These calculations have been carried out in both the Se-poor and Se-rich regimes using the HSE06 + D3 method, including separate calculations for the different Sb and Se sites (the importance of which was highlighted by Savory and Scanlon [6]). The formation energy of a Sn substitutional defect was calculated on each Sb site as well as a Sn interstitial defect, providing a comprehensive picture of defect formation upon inclusion of Sn impurities.

Figure 7. Transition level diagrams for Sn-doped Sb_2Se_3 in the (a) Se-rich and (b) Se-poor regimes, plotting defect formation energy (eV) against position of the Fermi level above the valence band maximum. Defect charge states are given by the slope of the lines, with transition levels represented by filled circles.

In the Se-rich regime (figure 7(a)), Sn_{Sb} substitutional defects have the lowest formation energy in the mid gap region, acting as acceptors with a 1− charge state, but transitioning to donor behaviour (1+) at Fermi level energies of 0.389 eV and 0.25 eV above the VBM, for Sb1 and Sb2 sites respectively. Sb is, of course, a group XV element that exists in the 3+ oxidation state when bonded in Sb_2Se_3 due to the lone pair effect [13]. Sn, similarly, is a group XIV element that can exist in the 2+ oxidation state under certain conditions. Sn in the 2+ oxidation state occupying an Sb site would act as an acceptor, whereas any Sn atoms in the 4+ oxidation state would instead act as a donor. This transition at 0.4 eV would cause the Fermi level to be pinned and could impose a limit on how high a carrier density is achievable for this system. In the Se-poor regime (figure 7(b)) the formation energies of Sn_{Sb} defects are lower but the transitions from

acceptor to donor behaviour occur at approximately the same Fermi energy. However, in the Se-poor regime they are also crossed by the Sn_i interstitial defect at ~0.45 eV above the VBM, as well as the Sb_i at slightly lower energy, which both exhibit donor behaviour (2+ for Sn_i, 3+ for Sb_i). This indicates a self-compensation mechanism between Sn_{Sb} and Sn_i, on top of the pinning already caused by the transition of the Sn_{Sb} from 1− charge state to the 1+ charge state. The Se-poor regime shows pinning occurring slightly higher in the band gap than for the Se-rich regime due to the lower formation energy of Sn_i interstitial states. This is in good agreement with the Hall effect measurements in which higher carrier densities were measured for the Se-rich regime than for the Se-poor regime.

4. Discussion

The question of effective routes for extrinsic p-type doping of Sb_2Se_3 is an active and fast-moving area of research for device applications. The hot-probe measurements taken in this work for undoped crystals provide more evidence that p-type conductivity can be achieved with a Se-excess, much as was observed by Chen *et al* [38], as a result of shallow V_{Sb} defects. However, we observed low conductivities which are consistent with the low carrier densities reported elsewhere, supporting the idea that intrinsic hole densities are low and extrinsic doping is necessary to achieve high hole concentrations. Furthermore it can be inferred from the lack of observable conductivity in the Se-poor sample in this work that defects associated with this composition, e.g. V_{Se}, did not contribute to n-type doping and were therefore primarily deep-level carrier traps or recombination centres. This is contrary to the proposal of an Sb-excess as a route to n-type conductivity [1]. Meanwhile, Sn-doping was comprehensively shown to induce p-type conductivity: our samples used high-purity bulk crystal materials and so we were able to eliminate the effects of uncontrolled impurities as well as the grain boundaries that may influence thin films. Moreover, Sn-doping induced p-type conductivity in not only Se-rich, but also Se-poor and even (previously n-type) Cl doped samples. This provides further evidence that Sn is capable of acceptor doping to induce p-type conductivity in samples where donor defects would ordinarily be observed (or expected, in the case of V_{Se} for Se-poor undoped material).

These results are consistent with DFT that predicts p-type conductivity due to Sn_{Sb} acceptors, while also predicting that the Se-rich regime is more favourable for this. While the photoemission results showed higher 'bulk' carrier densities than the other techniques, this can be attributed to the fact that, despite the use of higher photon energies, leading to photoelectrons with higher IMFP, even HAXPES still only probes the top 30 nm (at most) of the samples, which may differ from the bulk carrier behaviour. Furthermore, the photoemission results contained in this work indicate that despite p-type conductivity in the bulk, an inversion layer was observed at the Sb_2Se_3–vacuum interface. This is an important point, as it means that p-type samples may be mistakenly identified as n-type if UPS alone is used to determine the conductivity type. Whether this inversion layer may exist at other interfaces, such as those present in a solar cell, is a matter for future work to consider. As such, this work demonstrates the utility of using different photoemission energies to probe different depth regions in Sb_2Se_3, as well as the value of a DOS fit to band edges (as opposed to a linear edge fit), allowing the surface space-charge region to be modelled with the Poisson equation.

Carrier density measurements from Hall effect and *C–V* suggest a maximum carrier density of 7.4×10^{14} cm^{-3}, for a sample with both a Se-excess and Sn-doping at a concentration of 0.1 mol%. It is important to consider whether the carrier type inversion layer identified via photoemission could have led to an underestimate of the net hole density in Hall effect measurements (in the van der Pauw geometry) due to surface electrons. This may partially explain the different value resulting from the Poisson equation fit, but it is worth noting that this layer was not expected at the In–Sb_2Se_3 Schottky interface used for *C–V* measurements, and so the fact that the *C–V* measurements also indicated a carrier density on the order of 10^{14}, suggests this figure is accurate. Overall, quantifying the likely impact of the carrier type inversion layer upon the Hall effect measurements is beyond the scope of this work, and its possible impact cannot be ruled out in future work. However, assuming this hole density is accurate, it represents a low activation ratio, which is consistent with the compensation and Fermi-level pinning predicted by DFT. The fact that Sn may assume the Sn^{4+} oxidation state in addition to the Sn^{2+}, offers the possibility of Sn_{Sb} transitioning from the 1− to the 1+ charge state and providing a route for compensation. This is in addition to compensation due to the formation of Sn interstitials. It is possible, however, that the large concentration of Sn (7×10^{18} cm^{-3}) compared to conventional doping levels, exacerbated the issue of compensation, and smaller Sn quantities could conceivably produce greater activation efficiency and higher hole densities, but this has yet to be investigated. Conversely, other works have reported the highest level of p-type doping with much larger Sn concentrations than those used here (up to 10 mol% [39]). XRD characterisation in that work suggested that

Sb_2Se_3 can tolerate a high Sn concentration without the formation of secondary phases, with Hume-Rothery rules given as the explanation. This is feasible since the difference in atomic radii between Sb and Sn is less than 15% [40]. However, even if secondary phases were not observed, that report still represents a departure from doped Sb_2Se_3 to a mixed $(Sn,Sb)_2Se_3$ solid solution, which is likely to have significantly different properties. This may explain the high carrier density reported, in spite of Fermi-level pinning expected from DFT in this work, as the DFT was limited to Sn-doped Sb_2Se_3, rather than a solid solution. Further study will be necessary to determine if such a solid solution is well suited to PV solar cells more generally. To our knowledge, there are no reports at present of these large Sn concentrations being applied in a conventional heterojunction device (as opposed to the homojunction reported by Chen *et al* [39]). Returning to doped Sb_2Se_3, a low activation ratio for Sn has also been reported in single crystals in the past, using a greater concentration of Sn than in this work (0.5–1 mol%) [9], suggesting that larger Sn concentrations than in this work did not significantly increase the hole density, consistent with dopant compensation. Future studies of the compensation curve of Sn doping could determine an optimal Sn concentration to produce greater carrier densities than those observed in this work. Lower concentrations of Sn could also improve the values of carrier mobility, given that the values measured in this work (see table 2) were significantly lower than the largest values reported in the literature (20–40 $cm^2\,V^{-1}\,s^{-1}$) [1]. The samples in this work were intended to contain significant densities of native defects (due to Se or Sb excesses during synthesis) and/or substitutional defects from impurities (Cl and Sn) so that their effects on the majority carrier type were clear, but the over-doping with Sn may have contributed carrier traps that reduced mobility. Additionally, since previous photoluminescence [4] and deep-level transient spectroscopy [3] studies have suggested there are deep-level native defects within Sb_2Se_3, future work that aims for stoichiometric samples as well as reducing dopant concentration may improve on these values of mobility.

While there may be scope to increase the hole densities over those observed here, our DFT results suggest that whatever quantity of Sn is used, self-compensation of Sn_{Sb} and Fermi-level pinning could continue to restrict Sn-doping. This makes the consideration of alternative p-type dopants worthwhile.

When considering alternative p-type dopants, there are issues reported with using dopant atoms that are significantly smaller than the Sb or Se atoms on their intended substitution site, as these may form interstitial defects instead. Indeed, Huang *et al* argued that interstitial formation is more likely in a van der Waals structured material such as Sb_2Se_3 [41]. They suggest it as an explanation for why doping attempts using Cu and Zn have been unsuccessful to date. Interstitials may also explain the n-type conductivity reported as a result of Fe-doping [1]. It was partly as a response to these limitations that Huang *et al* made use of Pb as a p-type dopant, as its large atomic radius was expected to make interstitial formation unlikely. P-type conductivity and carrier densities ranging from 10^{13} to 10^{15} cm^{-3} with increasing Pb were observed at room temperature. This level of doping represents an improvement over the levels achieved with Sn in this work, and is consistent with Bacewicz *et al* [9], where greater conductivity was observed in Pb-doped Sb_2Se_3 crystals than in Sn-doped. This does not exceed the carrier densities reported for a $(Sn,Sb)_2Se_3$ solid solution [39], but in the report on Pb-doping, bulk samples were shown to reach carrier densities of 10^{18} cm^{-3}, with limited transfer of Pb from the source given as the explanation for the lower values in the thin films. Importantly, despite the increased hole density in the Sb_2Se_3 films compared to undoped Sb_2Se_3, device efficiency dropped, suggesting that the Pb may have also introduced deep-level defects. This, along with challenges in the incorporation of Pb via vapour-based methods, may represent the main limitations of Pb-doping at present. These works provide an important platform for the optimisation of p-type doping in Sb_2Se_3 solar cell devices and studies on this are ongoing.

5. Conclusion

This work provides, via photoemission, hot-probe and Hall effect measurements, strong evidence for Sn as a p-type dopant in bulk crystal Sb_2Se_3, most likely via Sn_{Sb}, and demonstrating higher conductivity than that observed as a result of V_{Sb} alone. Photoemission also demonstrates the presence of a majority carrier type inversion layer at the surface of these crystals, which could be fitted with a solution to Poisson's equation. The maximum hole density observed, at 7.4×10^{14} cm^{-3}, was lower than the ideal level for solar PV ($\sim 10^{16}$ cm^{-3}), at least for the Sn-concentrations used in this work. Indeed, since the chemical concentration was 7×10^{18} cm^{-3} here, fewer than one in 10 000 Sn atoms contributed to the net carrier density. In the absence of a full study of carrier vs dopant concentration it is not possible to say whether more or less Sn will be required to reach the highest hole concentrations. Fermi-level pinning may provide an obstacle to Sn doping, making it prudent to also investigate alternative dopants such as Pb, but the reliable route to p-type conductivity demonstrated for Sb_2Se_3 in this work is expected to have many applications both within and outside the field of solar PV.

Data availability statement

The data that support the findings of this study are openly available at the following URL/DOI: https://datacat.liverpool.ac.uk/id/eprint/1702 [33].

Acknowledgments

ORCID iDs

Theodore D C Hobson ⓘ https://orcid.org/0000-0002-0013-360X
Matthew J Smiles ⓘ https://orcid.org/0000-0003-2530-5647
Guillaume Zoppi ⓘ https://orcid.org/0000-0003-3622-6899
Tim D Veal ⓘ https://orcid.org/0000-0002-0610-5626
Ken Durose ⓘ https://orcid.org/0000-0003-1183-3211

References

[1] Mavlonov A *et al* 2020 A review of Sb_2Se_3 photovoltaic absorber materials and thin-film solar cells *Sol. Energy* **201** 227–46

[2] Spalatu N, Krautmann R, Keterski A, Kärber E, Josepson R, Hiie J, Acik I O and Krunks M 2021 Screening and optimization of processing temperature for Sb_2Se_3 thin film growth protocol: interrelation between grain structure, interface intermixing and solar cell performance *Sol. Energy Mater. Sol. Cells* **225** 111045

[3] Hobson T D C, Phillips L J, Hutter O S, Durose K and Major J D 2020 Defect properties of Sb_2Se_3 thin film solar cells and bulk crystals *Appl. Phys. Lett.* **116** 261101

[4] Grossberg M, Volobujeva O, Penežko A, Kaupmees R, Raadik T and Krustok J 2020 Origin of photoluminescence from antimony selenide *J. Alloys Compd.* **817** 152716

[5] Liu X *et al* 2017 Enhanced Sb_2Se_3 solar cell performance through theory-guided defect control *Prog. Photovolt., Res. Appl.* **25** 861–70

[6] Savory C N and Scanlon D O 2019 The complex defect chemistry of antimony selenide *J. Mater. Chem.* A **7** 10739–44

[7] Hobson T D C *et al* 2020 Isotype heterojunction solar cells using n-type Sb_2Se_3 thin films *Chem. Mater.* **32** 2621–30

[8] Liang G, Chen M, Ishaq M, Li X, Tang R, Zheng Z, Su Z, Fan P, Zhang X, Chen S 2022 Crystal growth promotion and defects healing enable minimum open-circuit voltage deficit in antimony selenide solar cells *Adv. Sci.* **9** 2105142

[9] Bacewicz R and Ciszek T F 1991 Liquid encapsulated crystal growth and electrical properties of Sb_2Se_3 and Bi_2S_3 *J. Cryst. Growth* **109** 133–6

[10] Stoliaroff A, Lecomte A, Rubel O, Jobic S, Zhang X, Latouche C and Rocquefelte X 2020 Deciphering the role of key defects in Sb_2Se_3, a promising candidate for chalcogenide-based solar cells *ACS Appl. Energy Mater.* **3** 2496–509

[11] Liang G *et al* 2021 Ion doping simultaneously increased the carrier density and modified the conduction type of Sb_2Se_3 thin films towards quasi-homojunction solar cell *J. Materiomics* **7** 1324–34

[12] Hobson T D C and Durose K 2021 Protocols for the miller indexing of Sb_2Se_3 and a non-x-ray method of orienting its single crystals *Mater. Sci. Semicond. Process.* **127** 105691

[13] Don C H *et al* 2020 Sb $5s^2$ lone pairs and band alignment of Sb_2Se_3: a photoemission and density functional theory study *J. Mater. Chem.* C **8** 12615–22

[14] Luo M, Leng M, Liu X, Chen J, Chen C, Qin S and Tang J 2014 Thermal evaporation and characterization of superstrate CdS/Sb_2Se_3 solar cells *Appl. Phys. Lett.* **104** 173904

[15] Fleck N, Hobson T D C, Savory C N, Buckeridge J, Veal T D, Correia M R, Scanlon D O, Durose K and Jäckel F 2020 Identifying Raman modes of Sb_2Se_3 and their symmetries using angle-resolved polarised Raman spectra *J. Mater. Chem.* A **8** 8337–44

[16] Haynes W M 2015 *CRC Handbook of Chemistry and Physics* 95th edn (Boca Raton, FL: CRC Press)

[17] Shirley D A 1972 High-resolution x-ray photoemission spectrum of the valence bands of gold *Phys. Rev.* B **5** 4709–14

[18] Kresse G and Hafner J 1993 *Ab initio* molecular dynamics for liquid metals *Phys. Rev.* B **47** 558–61

[19] Kresse G and Hafner J 1994 *Ab initio* molecular-dynamics simulation of the liquid-metal amorphous-semiconductor transition in germanium *Phys. Rev.* B **49** 14251–69

[20] Kresse G and Furthmüller J 1996 Efficient iterative schemes for *ab initio* total-energy calculations using a plane-wave basis set *Phys. Rev.* B **54** 11169–86

[21] Kresse G and Furthmüller J 1996 Efficiency of *ab-initio* total energy calculations for metals and semiconductors using a plane-wave basis set *Comput. Mater. Sci.* **6** 15–50

[22] Blochl P 1994 Projector augmented-wave method *Phys. Rev.* B **50** 17953–79

[23] Heyd J, Scuseria G E and Ernzerhof M 2003 Hybrid functionals based on a screened Coulomb potential *J. Chem. Phys.* **118** 8207–15

[24] Krukau A V, Vydrov O A, Izmaylov A F and Scuseria G E 2006 Influence of the exchange screening parameter on the performance of screened hybrid functionals *J. Chem. Phys.* **125** 224106

[25] Grimme S 2004 Accurate description of van der Waals complexes by density functional theory including empirical corrections *J. Comput. Chem.* **25** 1463–73

[26] Phillips L J *et al* 2019 Current enhancement via a TiO_2 window layer for CSS Sb_2Se_3 solar cells: performance limits and high V_{oc} *IEEE J. Photovolt.* **9** 544–51

[27] Freysoldt C, Neugebauer J and van de Walle C G 2009 Fully *ab initio* finite-size corrections for charged-defect supercell calculations *Phys. Rev. Lett.* **102** 016402

[28] Lany S and Zunger A 2008 Assessment of correction methods for the band-gap problem and for finite-size effects in supercell defect calculations: case studies for ZnO and GaAs *Phys. Rev.* B **78** 235104

[29] Murphy S T and Hine N D M 2013 Anisotropic charge screening and supercell size convergence of defect formation energies *Phys. Rev.* B **87** 094111

[30] Mahboob I, Veal T D, McConville C F, Lu H and Schaff W J 2004 Intrinsic electron accumulation at clean InN surfaces *Phys. Rev. Lett.* **92** 036804

[31] Shiel H 2021 Band alignments and interfaces in antimony selenide solar cells *PhD Thesis* University of Liverpool

[32] Shiel H *et al* 2021 Band alignment of Sb_2O_3 and Sb_2Se_3 *J. Appl. Phys.* **129** 235301

[33] Hobson T D C, Leighton C, Das B and Zoppi G 2022 Data consisting of: Hall effect, hot probe, SIMS and capacitance-voltage methods for paper: P-type conductivity in Sn-doped Sb_2Se_3 *DataCat Liverpool* (https://doi.org/10.17638/datacat.liverpool.ac.uk/1702)

[34] Blood P and Orton J W 1992 *The Electrical Characterisation of Semiconductors* (New York: Academic)

[35] Maurya K K and Singh V N 2021 Sb_2Se_3 versus Sb_2S_3 solar cell: a numerical simulation *Sol. Energy* **228** 540–9

[36] Zhang X *et al* 2017 Potential resolution to the doping puzzle in iron pyrite: carrier type determination by Hall effect and thermopower *Phys. Rev. Mater.* **1** 015402

[37] Tanuma S, Powell C J and Penn D R 1991 Calculations of electron inelastic mean free paths. III. Data for 15 inorganic compounds over the 50–2000 eV range *Surf. Interface Anal.* **17** 927–39

[38] Chen Z, Guo H, Ma C, Wang X, Jia X, Yuan N and Ding J 2019 Efficiency improvement of Sb_2Se_3 solar cells based on la-doped SnO_2 buffer layer *Sol. Energy* **187** 404–10

[39] Chen S, Qiao X, Zheng Z, Cathelinaud M, Ma H, Fan X and Zhang X 2018 Enhanced electrical conductivity and photoconductive properties of Sn-doped Sb_2Se_3 crystals *J. Mater. Chem.* C **6** 6465–70

[40] Callister W D and Rethwisch D G 2011 *Materials Science and Engineering* (New York: Wiley)

[41] Huang M, Lu S, Li K, Lu Y, Chen C, Tang J and Chen S 2021 P-type antimony selenide via lead doping *Sol. RRL* **6** 2100730